Chemical Engineering Journal 420 (2021) 129990

Contents lists available at ScienceDirect

Chemical Engineering Journal

journal homepage: www.elsevier.com/locate/cej

Effect of amino acid-derived nitrogen and/or sulfur doping on the visible-light-driven antimicrobial activity of carbon quantum dots: A comparative study

Jun-Won Kang [a], Dong-Hyun Kang [a,b,*]

[a] Department of Food and Animal Biotechnology, Department of Agricultural Biotechnology, Center for Food and Bioconvergence, and Research Institute of Agricultural and Life Sciences, Seoul National University, Seoul 08826, Republic of Korea
[b] Institutes of Green Bio Science & Technology, Seoul National University, Pyeongchang-gun, Gangwon-do 25354, Republic of Korea

ARTICLE INFO

Keywords:
Carbon quantum dots
Visible light
Antimicrobial effect
Doping
Water disinfection

ABSTRACT

The purpose of this study was to investigate the effects of nitrogen and sulfur derived from amino acids on the visible-light-driven (VLD) antimicrobial activity of carbon quantum dots (CQDs) and to establish an optimal doping form. Various CQDs were synthesized by combining malic acid as a carbon source, alanine containing N, and cysteine containing N and S through microwave heating. The results showed that the VLD antimicrobial activity of the CQD against Gram-positive (*Staphylococcus aureus* and *Listeria monocytogenes*) and Gram-negative pathogens (*Escherichia coli* O157:H7 and *Salmonella* Typhimurium) was improved by N and/or S doping, which increased as the ratio of S decreased. The doping of N and/or S made CQDs have a lower band gap energy, and CQD doped with only N (N-CQDs) exhibited greater specific surface area and fluorescence quantum yields (FLQYs), and longer photoluminescence (PL) lifetimes than CQD doped with N and S (NS-CQDs) even though NS-CQD and N-CQD had similar hand gap energies. Based on these results, the mechanism by which the VLD antimicrobial activity of CQD changes by doping was discussed. Furthermore, this study suggests that for CQD synthesis using food by-products, the more amino acids that can induce the doping of N and/or S, wherein the smaller ratio of S containing amino acids, the better VLD antimicrobial activity the synthesized CQD will have.

1. Introduction

Water is an essential resource for life activity, but when it is contaminated with pathogenic microorganisms, it poses serious harm to human health. Annually millions of people die from waterborne pathogen infections, of which most are children under 5 years old [1,2]. Accordingly, the World Health Organization stipulates that the concentration of pathogenic bacteria in drinking water should be <100 colony forming units (CFU)/mL [3]. Over the last century, public infrastructure for drinking water, which consists of a centralized water treatment system and an underground water distribution network using pipelines, has been established to effectively suppress the occurrence of diseases and improve public health and welfare [1]. However, approximately 1 billion people, most of which are low-income people living in rural areas, do not have access to safe water because they do not have access to this basic drinking water system environment [4,5]. In particular, it is estimated that >80% of disease incidences in developing countries may be related to waterborne pathogens [6].

Conventionally, chemical disinfectants, such as chlorine, chlorine dioxide, chloramines, and ozone, are used for water disinfection as they effectively oxidize pathogens and eventually induce death [4]. However, these disinfectants pose an inherent problem as they can react with other substances to form toxic disinfection by-products [7]. Therefore, many drinking water facilities are switching to use ultraviolet (UV) disinfection [4]. However, UV technology requires a high upfront cost to build a facility or operate and consumes a large amount of energy that contributes to global warming [8–10]. Thus, it is necessary to develop a water disinfection technology that is sustainable, low in cost, eco-friendly, safe, and exhibits high microbial control effects [8].

Visible-light-driven (VLD) photocatalysis disinfection technology is regarded as a promising water disinfection technology because it can control pathogens using natural light, such as sustainable sunlight and indoor lights. This technology directly kills pathogens by generating highly reactive species, such as holes (h^+), electrons (e^-), singlet oxygen

* Corresponding author at. Department of Agricultural Biotechnology, Seoul National University, Seoul 08826, Republic of Korea.
E-mail address: kang7820@snu.ac.kr (D.-H. Kang).

https://doi.org/10.1016/j.cej.2021.129990
Received 24 February 2021; Received in revised form 14 April 2021; Accepted 17 April 2021
Available online 23 April 2021

($^1O_2$), superoxide anion radicals ($\cdot O_2^-$), hydroxyl radicals ($\cdot$OH), and hydrogen peroxide (H_2O_2), that induce cell membrane destruction, DNA damage, protein oxidation, and lipid peroxidation, etc. by exciting e^- in the valence band (VB) of the semiconductor photocatalyst to the conduction band (CB) by photon energy [7,11]. Most of the studied catalysts that can effectively control pathogens under visible light are either single metal-based catalysts or co-catalysts containing more than one metal [12–19]. However, these metal-based photocatalysts are limited in practical applications because they are expensive to manufacture. Moreover, they have the potential to release toxic metallic ions under aqueous conditions [20]. Natural and synthetic photocatalysts can also be utilized for pathogen control, but they have several drawbacks, such as complex synthetic processes, difficulty in purification, high cost, and low water dispersibility and biodegradability [21].

As an alternative to these photocatalysts, carbon quantum dots (CQDs), which are a new type of carbon-based nanoparticle with photocatalytic and optical characteristics, are attracting increasing attention [22]. The first CQD was accidentally discovered in 2004 while separating and purifying single-walled carbon nanotubes [23], and in 2006 it was scientifically designated as a CQD by the research team of Sun et al. (2006), who studied surface passivation to improve their fluorescence [24]. CQDs are quasi-spherical nanoparticles with diameters of 10 nm or less composed of a nanocrystalline nucleus formed mainly by sp^2 hybridization of carbon that provides a quantum confinement effect to act as a semiconductor, a shell formed by sp^3 hybridized, and a functional group related to surface defects [25–27]. As CQDs have outstanding characteristics of high stability, eco-friendly, negligible toxicity, strong luminescence, biocompatibility, absorption of a wide range of wavelengths, high water dispersibility, and easy to synthesize on a large scale at low cost, research in various fields, including photocatalysis, electrocatalysis, chemical sensing, bioimaging, drug delivery, and photodynamic therapy, has been conducted [21,28–35]. In particular, CQDs have recently been shown to exhibit antimicrobial effects when activated in visible light, which means that pathogens can be controlled using light energy that can be easily utilized anywhere, such as sunlight or indoor light, by using CQDs [22].

CQD synthesis can be categorized into top-down or bottom-up routes. The top-down route is a method of splitting large-sized carbon materials, such as carbon nanotubes, graphite powder, carbon soot, and activated carbon, into small-sized CQDs via chemical oxidation, electrochemical carbonization, or laser-ablation. However, this method is expensive, complex, and not environmentally friendly [31,36,37]. Conversely, the bottom-up route is a method of synthesizing CQDs using small precursors, such as organic acids, amino acids, or natural materials, that contain carbon through hydrothermal, chemical, plasma, microwave, and solvothermal treatments, etc. Compared with the top-down route, this method is preferred because it is more convenient to synthesize, can be produced in large quantities at low cost, and is environmentally friendly [31,36,38]. Specifically, because waste generated through food production is currently emerging as a global environmental problem, if these food by-products, which are not valuable to use and cause environmental problems, are used for CQD synthesis, which is a material with high utilization value, it will not only help solve environmental problems but also generate significant economic benefits [39].

The intrinsic properties of CQDs, such as their electrical, optical, or chemical properties, change when the carbon framework or the chemical structure of the CQD surface is adjusted by doping with other elements, such as nitrogen, boron, sulfur, phosphorus, and carbon [40,41]. Food by-products can contain various amino acids, of which all amino acids contain C and N, and two amino acids (methionine and cysteine) contain S [42]. This means that depending on the type of food by-product, the form in which N and/or S are doped varies, and thus, various forms of CQD can be synthesized. Therefore, establishing the optimal doping form of N and S for synthesizing CQDs with the most effective VLD antimicrobial activity is pertinent for selecting the most suitable form of food by-products. However, to date, studies on the antimicrobial effect of CQDs according to the doping types of N and S have not been performed. Therefore, this study aimed to suggest an optimal doping form by comparing and analyzing the antimicrobial effects of undoped CQD, N-doped CQD, and N, S co-doped CQD against Gram-positive (*Staphylococcus aureus* and *Listeria monocytogenes*) and Gram-negative pathogens (*Escherichia coli* O157:H7 and *Salmonella* Typhimurium).

Table 1
Composition ratios of DL-Malic acid, L-Alanine, and L-Cysteine for the synthesis of undoped-carbon quantum dot (CQD), N-CQD, and NS-CQD.

Type of CQD	DL-Malic acid (g, mmol)	L-Alanine (g, mmol)	L-Cysteine (g, mmol)
Undoped-CQD	1.34 g, 10 mmol	–	–
N-CQD	1.34 g, 10 mmol	0.890 g, 10 mmol	–
NS-CQD	1.34 g, 10 mmol	0.872 g, 9.8 mmol	0.024 g, 0.2 mmol
	1.34 g, 10 mmol	0.801 g, 9.0 mmol	0.121 g, 1.0 mmol
	1.34 g, 10 mmol	0.445 g, 5.0 mmol	0.605 g, 5.0 mmol

2. Experiments

2.1. Synthesis of CQD

For CQD synthesis, DL-Malic acid (Sigma-Aldrich, St. Louis, MO, USA) was used as a carbon source, and L-alanine (Sigma Aldrich) containing N and L-cysteine (Sigma Aldrich) containing N and S were utilized for N and/or S doping. In particular, as cysteine has the same amount of C, H, O, N, as alanine, but more S, it is possible to change only the content of S without changing the amount of other atoms when synthesizing CQDs using only these two amino acids. For the synthesis of undoped-CQD, N-doped CQD, and N, S co-doped CQD, DL-Malic acid, L-alanine, and L-cysteine were combined, and their composition ratios are summarized in Table 1. Each combination was dissolved in 10 mL of ultrapure distilled water in a 50 mL Erlenmeyer flask and homogenized for 10 min by stirring. The completely homogenized solution was placed in a domestic microwave (700 W) and reacted for 5 min at maximum power, and then cooled to room temperature ($22 \pm 2^\circ$C). Then, 10 mL of ultrapure distilled water was added to the reacted solid product, which was dissolved in a 70°C water bath for 30 min, and centrifuged at 10,000 g for 20 min to obtain the supernatant. The supernatant was filtered again with a syringe filter (0.22 μm), and then dialyzed against ultrapure distilled water for 3 d through a dialysis membrane (MWCO 500 – 1000 Da), during which the ultrapure distilled water was changed every 24 h. The dialyzed solution was freeze-dried to obtain dried CQDs.

2.2. Characterization

Synthesized CQDs were characterized using various analytical instruments. Transmission Electron microscope (TEM) micrographs of CQDs and bacterial morphology were obtained using 200 kV TEM (JEM-F200, JEOL, Japan) and 120 kV TEM (Libra 120; Carl Zeiss, Germany), respectively. The particle size distribution of CQDs were determined through dynamic light scattering (DLS) uisng a Zetasizer Nano ZS (Malvern Instruments Ltd., Malvern, UK). Chemical structures of CQDs were analyzed using X-ray photoelectron spectroscopy (XPS, K-alpha, Thermo Scientific, UK) and Fourier-transform infrared spectroscopy

(FTIR, Nicolet 6700, Thermo Scientific, USA). The Photoluminescence (PL) spectra of the CQDs were recorded using a spectrofluorophotometer (Spectramax M2e; Molecular Devices, Sunnyvale, CA, USA). The true density of CQDs were measured using a gas pycnometer (AccuPyc II 1340, Micromeritics, Norcross, GA, USA). The Brunauer–Emmett–Teller (BET) analysis was performed using surface area analyzer (BELSORP-mini II, MicrotracBEL, Corp., Japan). The PL lifetime of CQDs was measured using a time-correlated single-photon counting (TCSPC) system (PicoHarp300, PicoQuant GmbH, Germany) and exponential fitting for the PL decays was achieved using Symphotime-64 software (Ver. 2.2).

2.3. Bacterial culture and inoculum preparation

Three strains each of *E. coli* O157:H7 (ATCC 43890, ATCC 43889, and ATCC 35150), *S.* Typhimurium (DT 104, ATCC 19585, and ATCC 43971), *L. monocytogenes* (ATCC 15313, ATCC 19111, and ATCC 19115), and *S. aureus* (ATCC 27213, ATCC 27649, and ATCC 25923) were provided by the Food Safety Engineering Laboratory at Seoul National University (Seoul, Republic of Korea) for use in this study. Stock and working cultures were prepared in the same method described in our previous study [43]. All the strains were cultured individually in 5 mL of tryptic soy broth (Difco, BD, Sparks, MD) at 37°C for 24 h, and cultured cells were harvested by centrifugation at 4,000 rpm for 20 min. After washing thrice with phosphate buffer saline (PBS), the final pellet was resuspended in PBS, and the suspended solutions of all the pathogens were combined to form a mixed culture cocktail containing approximately 10^9 – 10^{10} CFU/mL of each pathogen. This culture cocktail was used as the inoculum in this study.

2.4. Antimicrobial effect of CQD under visible light irradiation

Visible light was provided by a solar simulator (DXFL100, DTX Inc., Siheung, South Korea) with a xenon lamp (100 W) equipped with a UV cut-off lens (λ <400). Samples were prepared by placing 5.0 mL of ultrapure distilled water containing CQD at a concentration of 2 mg/mL and 0.1 mL of inoculum in a Petri dish (35 mm × 15 mm), closing the lid, and placing it at a vertical distance of 5 cm from the visible light source. The integral light intensity in the range of 400 – 800 nm at the sample surface was 7.8 mW/cm^2, which was measured with a fiber optic spectrometer (AvaSpec-ULS2048; Avantes, Eerbeek, Netherlands). The sample was treated with visible light at doses of 0 – 23.4 J/cm^2 (0 – 50 min) at room temperature (22 ± 2°C) while being mixed via pipetting at 10 min intervals. After treatment, 1 mL of treated sample was serially diluted 10-fold with 9 mL of sterile 0.2% peptone water (PW; Bacto, Becton and Dickinson) and 0.1 mL of diluent was spread onto the selective media. Sorbitol MacConkey Agar (Difco), Xylose lysine deoxycholate agar (Difco), Oxford agar base with Bacto Oxford antimicrobial supplement (Difco), and Baird Parker Agar (MB cell, Kisan Biotech Co., Ltd., Seoul, Korea) were used as selective media for the enumeration of *E. coli*, *S.* Typhimurium, *L. monocytogenes*, and *S. aureus*, respectively. All plates were incubated at 37°C for 24 h, and the typical colonies formed on the media were counted and calculated as $\log_{10}$ CFU/mL. In addition, dark control, including CQDs, but without visible light treatment, and light control with only visible light treatment without CQDs were evaluated using the same procedure.

2.5. Effect of reactive oxygen species (ROS) scavenger on CQD

ROS production related to the VLD antimicrobial activity of CQDs was determined by examining the VLD antimicrobial activity of CQDs in the presence of the ROS scavengers; sodium pyruvate, mannitol, sodium azide, and trion, which are scavengers of H_2O_2, ·OH, $^1O_2$, and $\cdot O_2^-$, respectively [44,45]. CQD solutions at a concentration of 2 mg/mL each, containing 5 mM sodium pyruvate, 50 mM mannitol, 5 mM sodium azide, and 5 mM Trion, were prepared, and their VLD antimicrobial effects were verified according to the procedure described in Section 2.4.

2.6. Destruction and lipid peroxidation occurrences in cell membrane

Propidium iodide (PI; Sigma Aldrich) and diphenyl-1-pyrenylphosphine (DPPP; Sigma-Aldrich), which are fluorescent dyes, were used to quantitatively evaluate the incidence of destruction and lipid peroxidation in the cell membrane, respectively. Five milliliters of distilled water containing CQDs at a concentration of 2 mg/mL inoculated with inoculum to obtain an optical density of 0.3 at 600 nm (OD_{600} = 0.3) was treated with visible light at a dose of 23.4 J/cm^2 (50 min) at room temperature (22 ± 2°C) while being mixed via pipetting at 10 min intervals. At this time, a light control that was treated with visible light without CQDs, and a dark control that included CQDs without visible light treatment were prepared. After treatment, cells were harvested by centrifugation at 10,000 g for 10 min, and washed three times with PBS. The final pelleted cells were incubated with PI or DPPP dye solutions at a concentration of 2.9 μM or 50 μM for 10 min or 20 min at 37°C, respectively. The incubated cell suspensions were centrifuged to harvest the reacted cells, washed twice with PBS, and the fluorescence was measured with a spectrofluorophotometer (Spectramax M2e) at excitation/emission wavelengths of 493/630 nm for PI, and 351/380 nm for DPPP. Destruction or lipid peroxidation in the cell membrane was determined as follows: [(Fluorescence value of visible light treated cells) – (Fluorescence value of dark-treated cells).

2.7. Band gap energy determination

The band gap energy (E_g) of the CQDs was determined using the Tauc model with the following equation:

$$\alpha h\nu = A\left(h\nu - E_g\right)^n$$

where A, α,h, and v are a constant, the absorption coefficient, Planck constant, and light frequency, respectively, and n = 1/2 and 2 are for the direct and indirect allowed transitions, respectively [46]. Specifically, for CQD, which is a direct allowed transition semiconductor, the $(\alpha h\nu)^2$

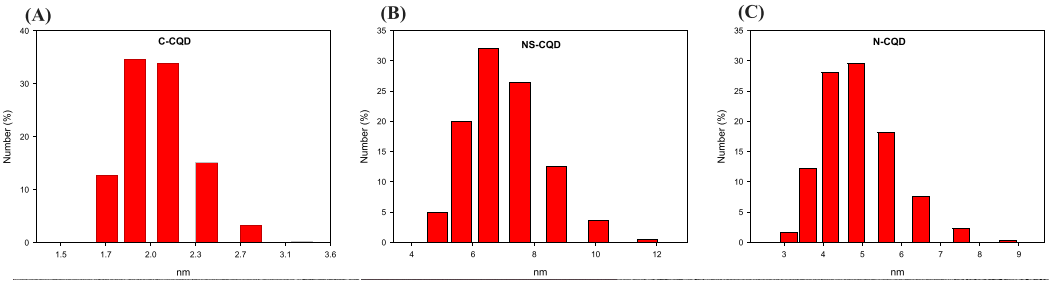

Fig. 1. Particle size distribution (%) and high-resolution transmission electron microscopy (HRTEM) images of carbon quantum dots (CQDs) synthesized with malic acid, alanine, and cysteine at ratios of (A) 10:0:0 mmol (C-CQD), (B) 10:5:5 mmol (NS-CQD), and (C) 10:10:0 (N-CQD), respectively.

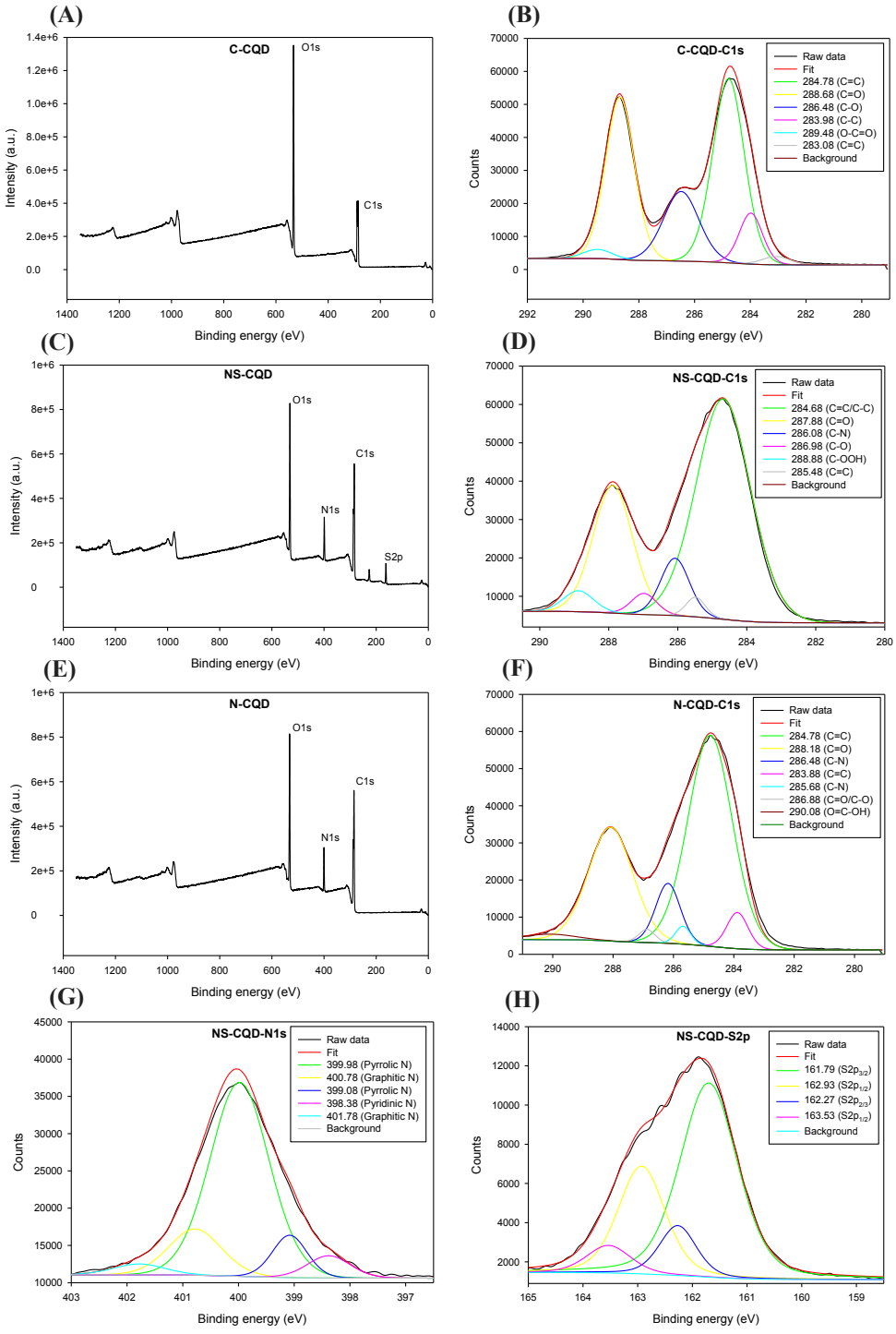

Fig. 2. X-ray photoelectron spectroscopy (XPS) spectra of carbon quantum dots (CQDs) synthesized with malic acid, alanine, and cysteine at ratios of (A) 10:0:0 mmol (C-CQD), (C) 10:5:5 mmol (NS-CQD), and (E) 10:10:0 (N-CQD), respectively. High resolution XPS spectra of the C1s of the (B) C-CQD, (D) NS-CQD, and (F) N-CQD, the N1s of (G) NS-CQD and (I) N-CQD, and the S2p of (H) NS-CQD, and (I) FTIR spectra of C-, NS-, and N-CQD.

versus *hv* (the incident photon energy) plot (Tauc plot) using the UV–vis absorption spectrum of CQD was obtained using the UV–Vis absorption spectrum, and the band gap energy was determined by measuring the intercept of the incident photon energy axis by extrapolating the straight part of the plot [47].

2.8. Fluorescence quantum yield (FLQY) measurement

The FLQY of the CQDs was measured with an established comparative method [48], wherein quinine sulfate (Sigma-Aldrich) dissolved in 0.1 M H_2SO_4 was selected as the reference standard (FLQY is 54%). The PL spectra of CQDs dissolved in ultrapure distilled water and quinine sulfate dissolved in 0.1 M H_2SO_4 in a 10 mm quartz cuvette were

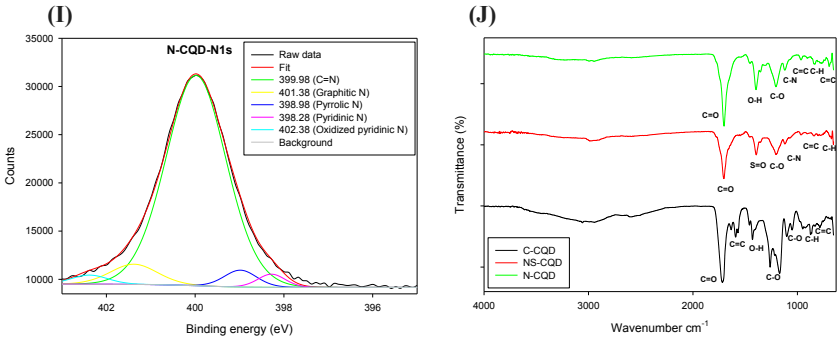

Fig. 2. (*continued*).

obtained at an excitation wavelength of 360 nm, and the integrated PL intensities were derived from the spectra. The absorbance values of the CQD and reference standard samples were kept below 0.1 to minimize the re-absorption effect. A plot of the integrated PL intensity versus its corresponding absorbance value was obtained, and the FLQY (%) was calculated as follows:

$$FLQY_x(\%) = FLQY_s(Grad_x/Grad_s)(\eta_s/\eta_x)$$

where × and s refer to CQD and quinine sulfate, respectively, Grad is the slope from the plot, η stands for the refractive index of the solvent, and η_x and η_s are both 1.33.

2.9. Statistical analysis

Experiments to evaluate the antimicrobial effect of CQDs under visible light irradiation, the occurrence of destruction and lipid peroxidation in the cell membrane, and the effect of reactive oxygen species (ROS) scavenger on CQD were independently repeated three times and the data were analyzed using an analysis of variance and the least significant difference (LSD) *t*-test using the Statistical Analysis System (SAS; Version 9.4. SAS Institute Inc., Cary, NC, USA). A probability level of $P < 0.05$ was used to determine significant differences.

3. Results and discussion

3.1. Characterization of synthesized CQDs

Fig. 1 shows the particle size distribution determined using the DLS technique of CQDs synthesized with malic acid, alanine, and cysteine, at ratios of 10:0:0 mmol (labeled as C-CQD), 10:5:5 mmol (labeled as NS-CQD), and 10:10:0 mmol (labeled as N-CQD), and the corresponding TEM images. Size distribution of C-, NS-, and N-CQDs have a typical CQD size of<10 nm, and their average sizes were 2.58, 6.95, 4.83 nm, respectively. Furthermore, it was observed that C-, NS-, and N-CQDs which have spherical structures with 0.25, 0.36, and 0.32 nm lattice spacing, which are similar to the facet (100), (002), (002) of graphite, respectively [49–51], which indicates that the CQDs synthesized in this study have the characteristics of a graphite sp^2 structure.

The surface state and functionality of the CQDs were confirmed by XPS and FTIR analyses (Fig. 2). C-, NS, and N-CQD all showed C1s and O1s peaks, NS-CQD additionally showed N1s and S2p peaks, and N-CQD additionally showed N1s peaks. The high-resolution C1s spectra of C-CQD show peaks at 284.78/283.08, 288.68, 286.48, 283.98, and 289.48 eV, corresponding to C = C, C = O, C-O, C–C, and O-C = O, respectively (Fig. 2B) [52–55]. For NS-CQD, the high-resolution spectra of C1s represent peaks of 284.68, 287.88, 286.08, 286.98, 288.88 and 285.48 eV, corresponding to C = C/C–C, C = O, C-N, C-O, C-OOH, and C = C, respectively (Fig. 2D) [56–58]. For N-CQD, the high-resolution spectra of C1s shows peaks of 284.78/283.88, 288.18, 286.48/285.68, 286.88, and 290.08 eV corresponding to C = C, C = O, C-N, C = O/C-O, and O = C-OH, respectively (Fig. 2F) [59–63]. The high-resolution spectra of N1s of NS-CQD revealed peaks at 399.98/399.08, 400.78/401.78, 398.38 eV, corresponding to pyrrolic-, graphitic-, and pyridinic N (Fig. 2G), respectively [64–66], and the S2p high-resolution spectra revealed peaks of 161.79/162.27 and 162.93/163.53 eV corresponding to $S2p_{3/2}$ and $S2p_{1/2}$, respectively (Fig. 2H), which can be attributed to S^{2-} [67–70]. The high-resolution spectra of N1s of N-CQD revealed peaks of 399.98, 401.38, 398.98, 398.28, and 402.38 eV, corresponding to C = N, graphitic, pyrrolic, pyridinic, and oxidized pyridinic N, respectively (Fig. 2I) [71,72]. Furthermore, FTIR spectrum analysis showed that C-CQD exhibited the absorption peaks of C = C bending (676 cm-1), C–H bending (874 cm-1), C-O stretching (1050, 1170, 1261 cm-1), O–H bending (1430 cm1-1), C = C stretching (1569, 1591, 1634 cm-1), C = O stretching (1717 cm-1) groups, N-CQD showed absorption peaks of C = C bending (696 and 965 cm-1), C–H bending (1702 cm-1) groups, while NS-CQD had absorption peaks of C = C bending (673, 801, 841 cm-1), C–H bending (782, 801 cm-1), C-N stretching (1120 cm-1), C-O stretching (1204 cm-1), S = O stretching (1394 cm-1), and C = O stretching (1703 cm-1) groups. XPS and FTIR results verified that C-, NS -, and N-CQDs were synthesized in a form in which un-, NS-, and N-doping were effectively induced.

3.2. VLD antimicrobial activity of C-, NS-, N-CQD

Fig. 3 shows the results of the antimicrobial effect of CQDs synthesized by varying the ratio of malic acid as a carbon source, alanine containing N, and cysteine containing both N and S under visible light. For all pathogens (*E. coli* O157:H7, *S.* Typhimurium, *L. monocytogenes*, and *S. aureus*), the CQD synthesized only with malic acid did not exhibit antimicrobial effects under visible light treatment, but when alanine and/or cysteine were doped to it, antimicrobial effects were observed. Specifically, the CQD synthesized by adding only 10 mmol of alanine to 10 mmol of malic acid exhibited the highest antimicrobial effect under visible light, and as the amount of cysteine added increased from 0.2 mmol to 5.0 mmol, the CQD antimicrobial effect proportionally decreased (Fig. 3A, C, E, and G). Meanwhile, none of the CQDs synthesized in this study showed antimicrobial effects under dark conditions for 50 min, which is the maximum amount of time visible light was applied in this study (Fig. 3B, D, F, and H). This result indicates that the addition of amino acids during CQD synthesis increases the VLD antimicrobial effect of CQD, but the effect decreases as the ratio of amino acids containing S increases. Several studies have reported that CQDs are driven by visible light to exert bactericidal effects, and the CQDs used in those studies were synthesized by adding N-containing 2,2′-(ethylenedioxy)bis(ethylamine) (EDA) or polyethylenimine to carbon nano-powder, a carbon source [22,29,73,74]. In particular, Rabe et al. (2019) synthesized CQDs by mixing EDA with amino groups ($–NH_2$) and 3-ethoxypropylamine (EPA) with methyl groups ($–CH_3$) with carbon nanopowder, respectively (referred to as EDA-Cdots and EPA-Cdots, respectively), confirming that EDA-Cdots showed greater visible light-

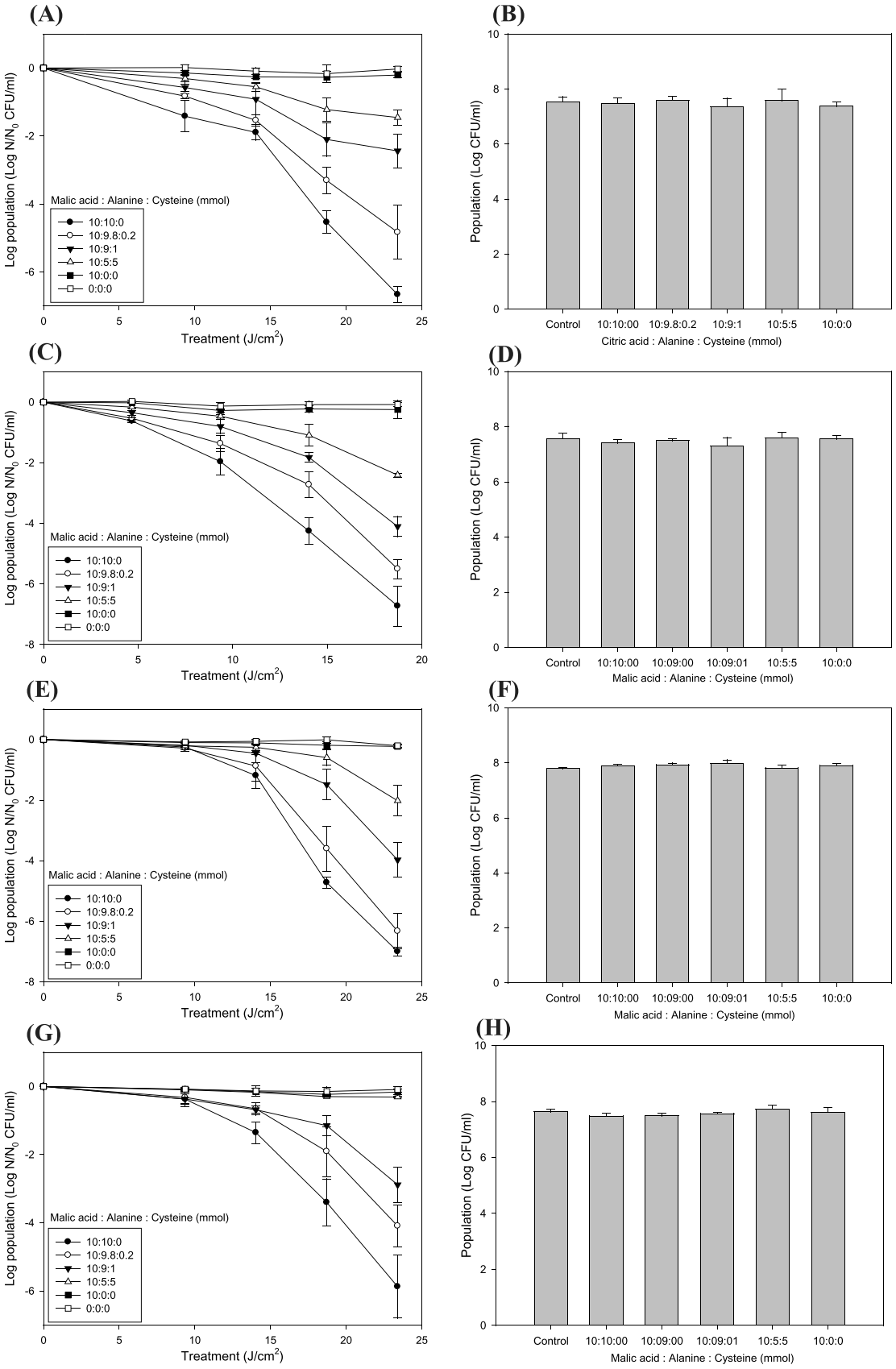

Fig. 3. Surviving populations (Log CFU/mL) of (A and B) *Escherichia coli* O157:H7, (C and D) *Salmonella* Typhimurium, (E and F) *Listeria monocytogenes*, and (G and H), *Staphylococcus aureus* subjected to treatment of 2 mg/mL of carbon quantum dots (CQDs) synthesized from various ratios of malic acid, alanine, and cysteine under visible light (A, C, E, G) or dark (B, D, F, H) treatments. Dark treatment was treated for 50 min, which is the same amount of time at which visible light was treated with 23.4 J/cm^2. The data indicate an average of three independent experiments and the standard deviations are shown by error bars.

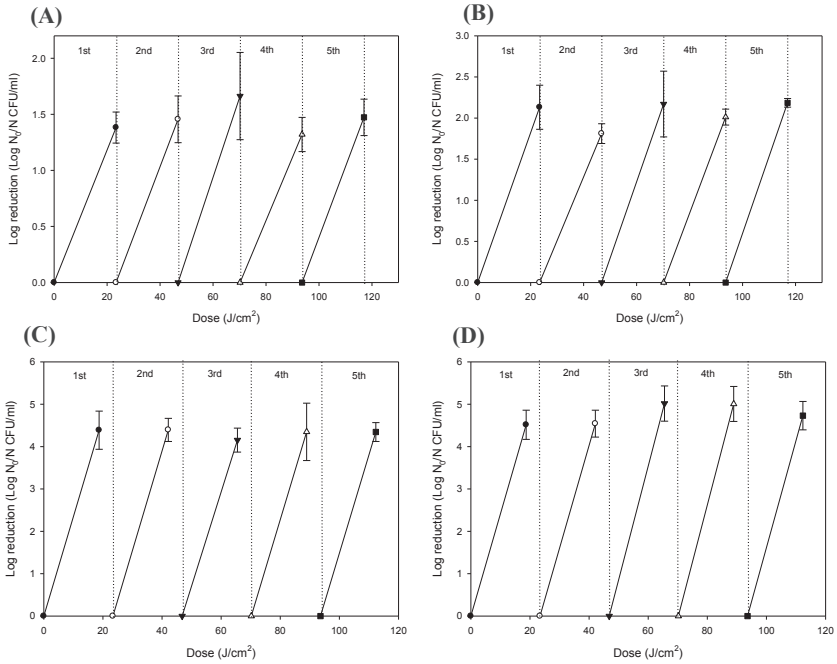

Fig. 4. Visible-light-driven antimicrobial activity of carbon quantum dots (CQDs) synthesized with malic acid, alanine, and cysteine at ratios of (A and B) 10:5:5 mmol (NS-CQD), and (C and D) 10:10:0 (N-CQD) for (A and C) *Escherichia coli* O157:H7 and (B and D) *Listeria monocytogenes* over five cycles of treatment. One cycle was 24.3 J/cm^2 (50 min) treatment, sampling was performed at 18.72 and 24.3 J/cm^2 for the N-CQD and NS-CQD treatments, respectively.

activated antimicrobial activity than the EPA-Cdots. Doping other elements to CQD can improve its application properties by adjusting their structure, composition, and improving its optical characteristics as doping can effectively change the CQD electronic properties or energy state [75,76].

In order to confirm the cyclic stability of CQDs with improved VLD antimicrobial activity by N- and/or S-doping, a 23.4 J/cm^2 treatment was performed as one cycle, and the stability change in NS- and N-CQD was confirmed over a total of five cycles of treatment. In this case, N-CQD was sampled after 18.72 J/cm^2 treatment to facilitate comparison, because the 23.4 J/cm^2 treatment of N-CQD reduced levels to almost below the detection limit. As shown in Fig. 4, neither NS- or N-CQDs exhibited significant ($P > 0.05$) changes in their VLD antimicrobial activity over five cycles, which means that N- and/or S-doped CQDs are highly reusable and can thus be utilized efficiently.

3.3. PL spectra

Fig. 5 shows the PL spectra of C-, NS-, and N-CQD. C-CQD showed that as the excitation wavelength increased from 300 nm to 400 nm, the peak emission wavelength hardly changed (from 458 nm to 464 nm, within 10 nm), and only the intensity changed (Fig. 5A). Meanwhile, NS- and N-CQD showed red-shifts in which the peak emission wavelength changed from 416 nm to 464 nm and from 416 nm to 460 nm, respectively, as the excitation wavelength increased (Fig. 5 B and C). Thus, with N and/or S doping, more surface defects as active sites with different energy levels are created, resulting in red-shift characteristics [77–79]. In particular, as these surface defects change the CQD properties, the CQD form can be improved through heteroatom doping [80–82], it can be inferred that the VLD antimicrobial effect of CQDs improves by changing the characteristics of CQD through the doping of N and/or S derived from amino acids.

3.4. Cell membrane damage

We investigated which CQD properties changed by N and/or S doping in order to determine which increased the VLD antimicrobial effect, and the cause of different effects depending on the type of doping. Dong et al. (2020) reported that CQDs generated damage in bacterial cell membranes under visible light [83]. Therefore, in our study, the degree of the cell membrane damage inductions of C-, N-, and NS-CQD were compared. PI is a dye that does not passes through the intact cell membrane owing to its size and charge properties, and it can pass through the cell membrane where destruction has occurred [84,85]. Thus, cell membrane damage was quantified based on the degree of PI uptake of cells. As shown in Fig. 6(A), under visible light treatment, C-CQD showed similar cell membrane destruction values to those treated with only visible light without CQD, but NS- and N-CQD significantly ($P < 0.05$) increased the cell membrane destruction value (except for NS-CQD on *S. aureus*) and N-CQD showed a greater significant ($P < 0.05$) increase than that of NS-CQD. When this type of cell membrane damage occurs, the cell cannot maintain homeostasis and thus, eventually dies [86,87] The results of the cell membrane destruction were consistent with those of the antimicrobial effects of CQD. Therefore, it can be interpreted that N and/or S doping increases the activity that induces cell membrane damage under visible light of CQD, which in turn increases the antimicrobial activity, in which N doping induces a greater increase than NS doping.

In addition, fatty acids are one of the most essential structures in cellular materials, and mainly exist in the cell membrane in the form of acyl of phospholipids [88]. When lipid peroxidation occurs in the cell membrane, the fluidity and potential difference of the fatty acid decreases, and its permeability increases [89] Thus, it is likely that cell membrane damage is related to lipid peroxidation. Therefore, the incidence of lipid peroxidation in the cell membrane was measured using DPPP, a dye that selectively reacts with lipid hydroperoxide in the cell membrane and is oxidized to DPPP = O, which is fluorescent [90]. As shown in Fig. 6(B), the degree of lipid peroxidation incidence by C-CQD under visible light was not significantly ($P > 0.05$) different from that of the cells treated with only visible light without CQD. Moreover, NS- and N-CQD had a significantly ($P < 0.05$) increased incidence of lipid peroxidation, wherein that of N-CQD was significantly ($P < 0.05$) greater than that of NS-CQD. This indicates that N and/or S doping increased the activity that induced lipid peroxidation under CQD visible light, and N

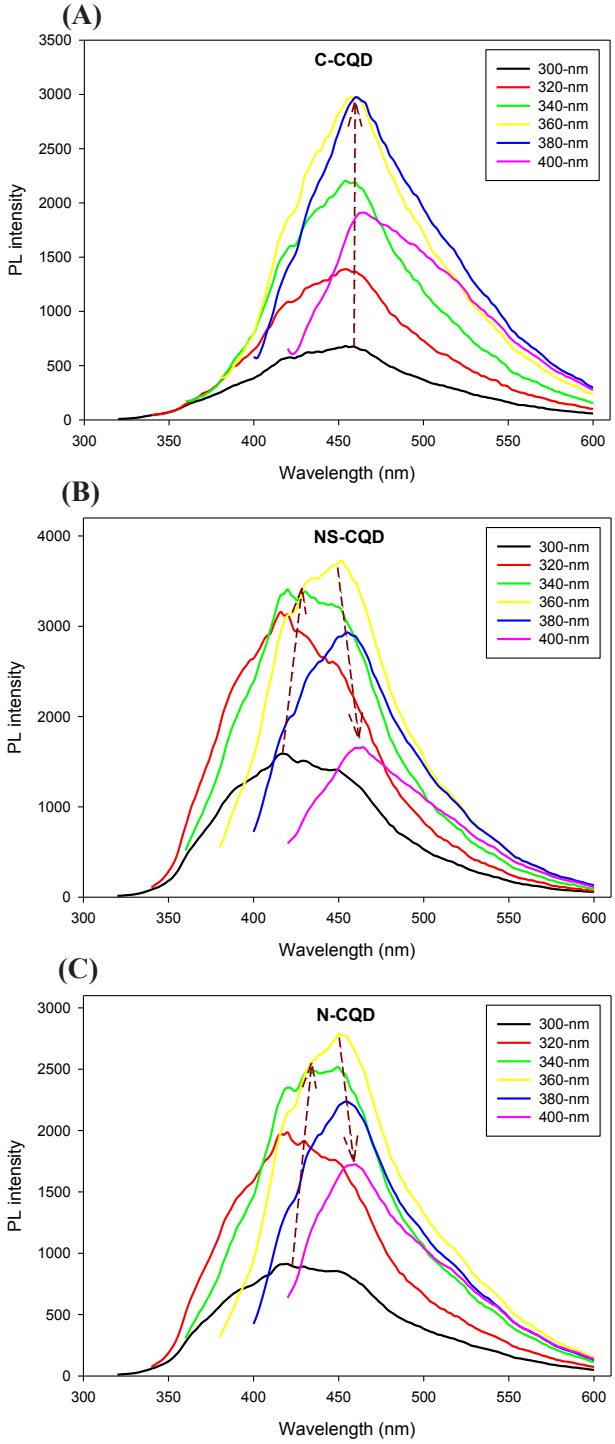

Fig. 5. Photoluminescence (PL) spectra taken at excitation wavelengths of 300 – 400 nm of carbon quantum dots (CQDs) synthesized with malic acid, alanine, and cysteine at ratios of (A) 10:0:0 mmol (C-CQD), (B) 10:5:5 mmol (NS-CQD), and (C) 10:10:0 (N-CQD), respectively.

doping had a higher activity than doping of N and S together.

In addition, the TEM image of *E. coli* O157:H7 after 23.4 J/cm^2 was observed to qualitatively analyze cell membrane damage. Fig. 7 shows the TEM image results showing the change in morphology of *E. coli* O157:H7 following C-, NS-, and N-CQD treatment. C-CQD showed a shape that was not significantly different from the untreated control, whereas after NS- and N-CQD treatment, the cell membrane was noticeably destroyed. These TEM results further reinforce the reliability

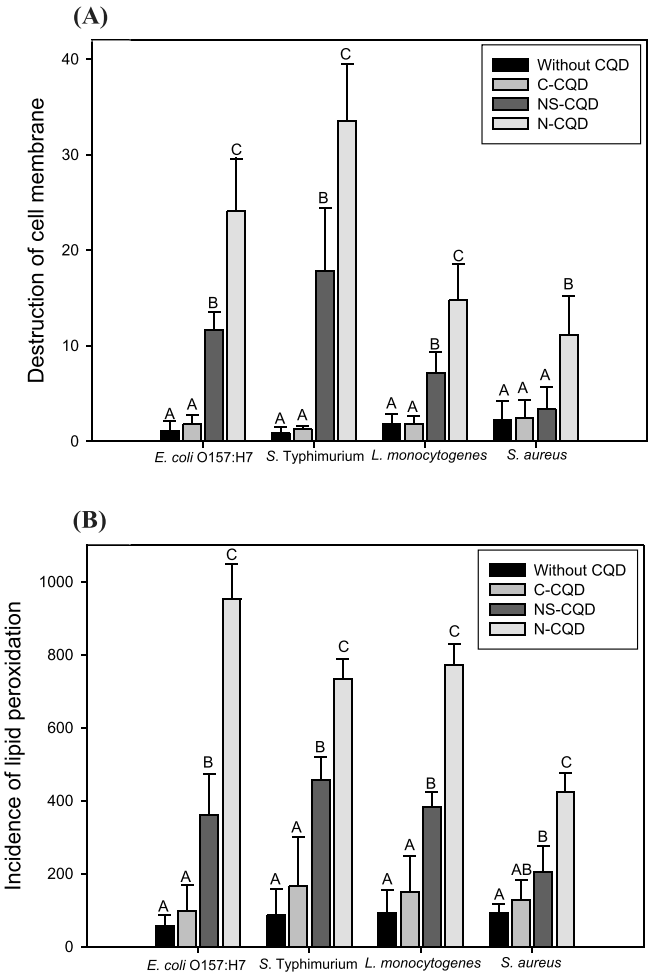

Fig. 6. . Values of (A) destruction and (B) lipid peroxidation incidence in cell membranes of *Escherichia coli* O157:H7, *Salmonella* Typhimurium, *Listeria monocytogenes*, and *Staphylococcus aureus* subjected to treatment of carbon quantum dots (CQDs) synthesized with malic acid, alanine, and cysteine at ratios of 10:0:0 mmol (C-CQD), 10:5:5 mmol (NS-CQD), and 10:10:0 (N-CQD). The values were obtained using: [(Fluorescence value of visible light treated cells) – (Fluorescence value of dark treated cells]. The data represent the averages of three independent experiments, and the error bars indicate the standard deviations. Different letters within the same pathogen indicate significant differences ($P < 0.05$).

of the VLD antimicrobial activity and cell membrane damage results.

3.5. Photocatalytic mechanism

Mechanically, when CQD is excited by light energy, charge separation that forms electrons and holes trapped in various passivated surface defect sites occurs extremely quickly, becoming an emissive excited state that is responsible for fluorescence emission via a radiative combination of these electron-hole pairs [22,83]. The photocatalytic reaction in the presence of water under aerobic conditions can generate several generating reactive oxygen species (ROS) from oxygen molecules and water [92]. It is known that excited photosensitizers can cause cell membrane damage by inducing lipid peroxidation by directly reacting with lipids or ROS that react with lipids [91]. Therefore, as CQDs can generate ROS through emissive excited states [22], the lipid peroxidation generated in this study was considered to be caused by the direct reaction of CQD excited by visible light and/or the ROS generated therefrom. To elucidate the photocatalytic mechanism of CQDs in detail, it is necessary to confirm the VB and CB energies, because the

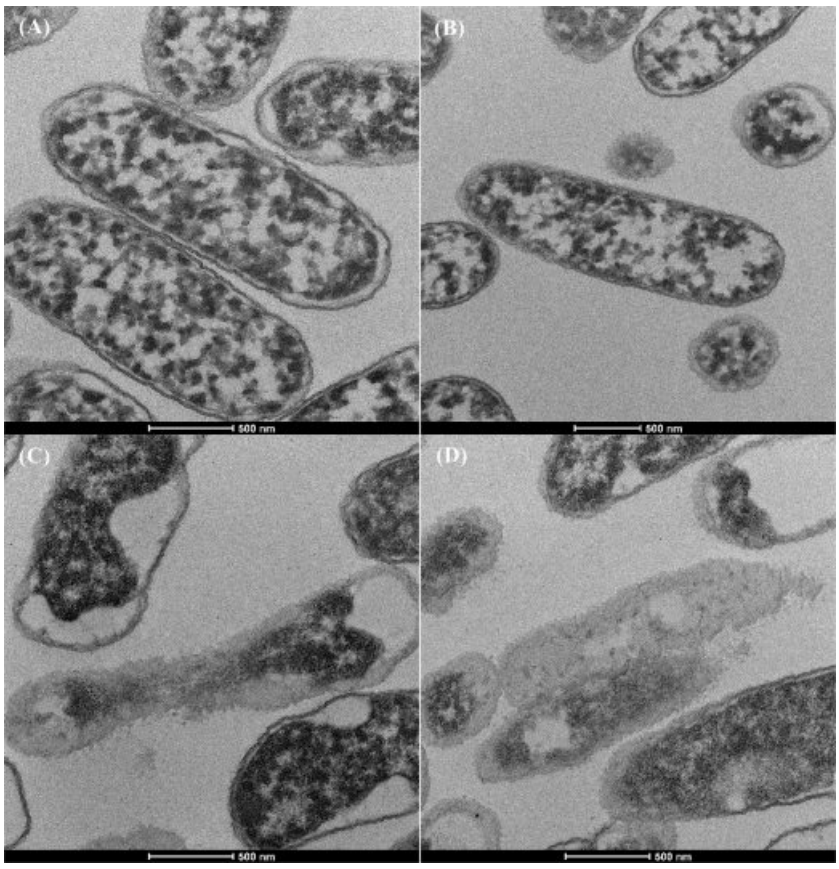

Fig. 7. Transmission electron microscope (TEM) micrographs of (A) untreated, carbon quantum dots (CQDs) synthesized with malic acid, alanine, and cysteine at ratios of (B) 10:0:0 mmol (C-CQD), (C) 10:5:5 mmol (NS-CQD), and (D) 10:10:0 (N-CQD) under visible light at dose of 24.3 J/cm^2 treated *Escherichia coli* O157:H7.

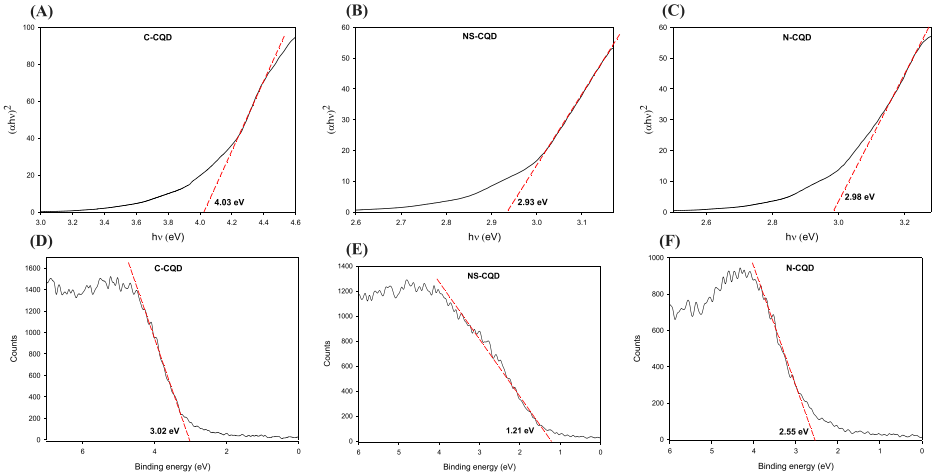

Fig. 8. Tauc plot [$(\alpha h\nu)^2$ versus $h\nu$] (A, B, and C) and XPS valence band spectra (D, E, and F) of carbon quantum dots (CQDs) synthesized with malic acid, alanine, and cysteine at ratios of 10:0:0 mmol (C-CQD), 10:5:5 mmol (NS-CQD), and 10:10:0 (N-CQD). α, h, and v are the absorption coefficient, Planck constant, and light frequency, respectively.

mechanism of ROS generation is different depending on the energy states of the separated electrons and holes [92]. Fig. 8 shows that C-, NS-, and N-CQD have band gap energies (E_g) of 4.03, 2.93, and 2.98 eV, respectively, and VB energy of 3.02, 1.21, and 2.55 eV (vs. NHE), respectively. By combining the E_g and VB energy data, the CB bands of C-, NS-, and N-CQD were −1.01, −1.72, and −0.43, respectively (vs. NHE), respectively. Using these data, Fig. 9 shows a schematic diagram of the photocatalytic mechanism of each C-, NS-, and N-CQDs. C-CQD has an E_g of 4.03 eV, which indicates that photoexcitation cannot be achieved by visible light, because visible light has<3.10 eV (>400 nm). Conversely, NS- and N-CQD have E_g values of 2.93 eV and 2.98 eV, respectively, which means that they can enter the photoexcitation state by excitation from visible light. However, they exhibit different photocatalytic mechanisms. Specifically, in the case of NS-CQD, because the CB energy has a greater negative potential than the $O_2/\cdot O_2^-$ pair, photo-activated electrons can transfer the π^* orbitals of oxygen molecules to produce

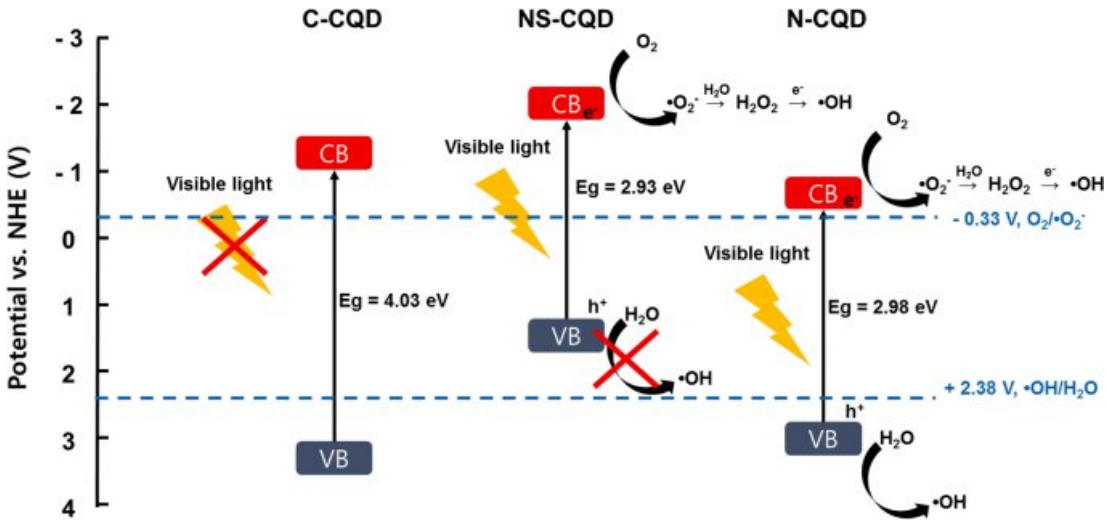

Fig. 9. Schematic diagram of photocatalytic mechanism of carbon quantum dots (CQDs) synthesized with malic acid, alanine, and cysteine at ratios of 10:0:0 mmol (C-CQD), 10:5:5 mmol (NS-CQD), and 10:10:0 (N-CQD). VB and CB are valence band and conduction band, respectively.

$\cdot O_2^-$, and this $\cdot O_2^-$ can subsequently be converted into several ROS, including H_2O_2 and $\cdot OH$ [92,93]. Because the VB energy shows a smaller positive potential than the $\cdot OH/H_2O$ pair, the generated h^+ cannot participate in the reaction to convert H_2O into $\cdot OH$. On the other hand, the CB energy of N-CQD is −0.43 eV, which has a greater negative potential than the $O_2/\cdot O_2^-$ pair and thus can generate $\cdot O_2^-$ and a series of related ROS, and at the same time, VB energy also has a greater positive potential than the $\cdot OH/H_2O$ pair, it is therefore possible to convert H_2O into $\cdot OH$.

To verify the occurrence of ROS, VLD antimicrobial activity was observed using a scavenger (Fig. 10). In order to facilitate comparison, visible light of 23.4 and 18.72 J/cm^2 was treated on NS- and N-CQDs, respectively. In the case of NS-CQD, the activity for *E. coli* O157:H7 was significantly ($P < 0.05$) decreased by H_2O_2 and $^1O_2$ scavengers, and for *L. monocytogenes*, the activity was significantly ($P < 0.05$) decreased by H_2O_2, $^1O_2$, and $\cdot O_2^-$ scavengers (Fig. 10A). The VLD antimicrobial activity of N-CQDs was significantly ($P < 0.05$) decreased in the presence of H_2O_2, $\cdot OH$, $^1O_2$, and $\cdot O_2^-$ scavenger, and the activity was markedly decreased by H_2O_2, $\cdot OH$, and $^1O_2$ scavengers for *E. coli* O157:H7 and by H_2O_2 and $^1O_2$ scavenger for *L. monocytogenes* (Fig. 10B). This result indirectly confirmed that a series of ROS can be effectively generated by VLD NS- and N-CQDs. In addition, it was confirmed that the sensitivity to ROS differs according to the type of pathogen (*E. coli* O157:H7 was more sensitive to $\cdot OH$ and $^1O_2$, while *L. monocytogenes* was more sensitive to H_2O_2 and $^1O_2$). Similarly, a study by Huang et al. (2012) reported that Gram-positive bacteria were more sensitive to $^1O_2$, while Gram-negative bacteria were more sensitive to $\cdot OH$ [94].

In terms of the band gap energy, N- and/or S-doped CQDs exhibited VLD antimicrobial activity, because the band gap energy of CQDs was reduced by N- and/or S-doping and thus became photo-excited by visible light. The decrease in the CQD bandgap energy by N- and/or S-doping could be explained as a reduction in the energy gap between the VB and CB by increasing the electron density near the CB by providing electrons to the CQD from the lone pair electrons of N or S [47,79,95]. Furthermore, the smaller the CQD bandgap energy, the more visible light can be harvested, and thus, light energy can be efficiently utilized, resulting in a higher antimicrobial effect. Indeed, Zhange et al. (2018) reported that chemically reduced graphene oxide quantum dots (rGOQDs), which are a reduced band gap energy form of graphene oxide quantum dots (GOQDs), produced a greater amount of ROS under visible light, resulting in a higher photodynamic therapy effect. However, this band gap energy result did not explain why N-CQDs exhibited a higher VLD antimicrobial effect than NS-CQDs, as the two had similar band gap energies (although NS-CQDs were slightly less than N-CQDs). Instead, unlike NS-CQDs, where photo-excited electrons convert O_2 to ROS, but h^+ does not react with H_2O, N-CQDs can react with both O_2 and H_2O to produce ROS, and therefore, this different photocatalytic mechanism may be related to different VLD antimicrobial activities.

3.6. Specific surface area

Nanoparticles show greater photocatalytic activity as their specific surface area increases, because the large specific surface area provides a large number of reactive sites, ensuring effective absorption of the reactant and incident light [96–98]. Thus, we performed the BET gas adsorption method to measure the specific surface area of the NS- and N-CQDs. The specific surface areas obtained through BET analysis of NS- and N-CQD were 0.77 and 1.58 m^2/g, respectively. Although this result showed that the specific surface area of N-CQDs was larger than that of NS-CQDs as expected, the specific surface area values of nano-sized N- and NS-CQDs were too small compared with CQDs synthesized in other study, which had a specific surface area of 200–500 m^2/g, depending on the synthesis conditions [99]. This difference is likely due to the aggregation of nanoparticles during the high-temperature degassing process of the BET analysis, which produced erroneous results. [100]. Therefore, in order to obtain more reliable results, we attempted to theoretically calculate the specific surface areas of NS- and N-CQDs using specific surface area (m^2/g) = 6000/(D*ρ), where D is the diameter of the particle in nm and ρ is the density of the particle in g/cm^3. The diameters of the NS- and N-CQDs were derived from Fig. 1, and their densities were measured using a gas pyconometer. As shown in Table 2, the specific surface areas (m^2/g) of NS- and N-CQD were estimated to be 571.73 and 850.85 m^2/g. Thus, it can be inferred that N doping acts to synthesize CQDs with a larger specific surface area than N and S co-doping, and reactive sites increase accordingly, thereby helping to show greater photocatalytic activity.

3.7. FLQY

CQDs can emit fluorescence through a series of processes, including: (1) electron-hole pairs generated by photoexcitation, which form emissive excited states while competing with other deactivation pathways; and (2) emitting fluorescence from emissive excited states while competing with non-radiative decay pathway [101]. The combination of the yield of the former process (Φ_1) and that of the latter (Φ_2) is reflected in the observed FLQY (Φ_F), which is determined using: $\Phi_F = \Phi_1\Phi_2$.

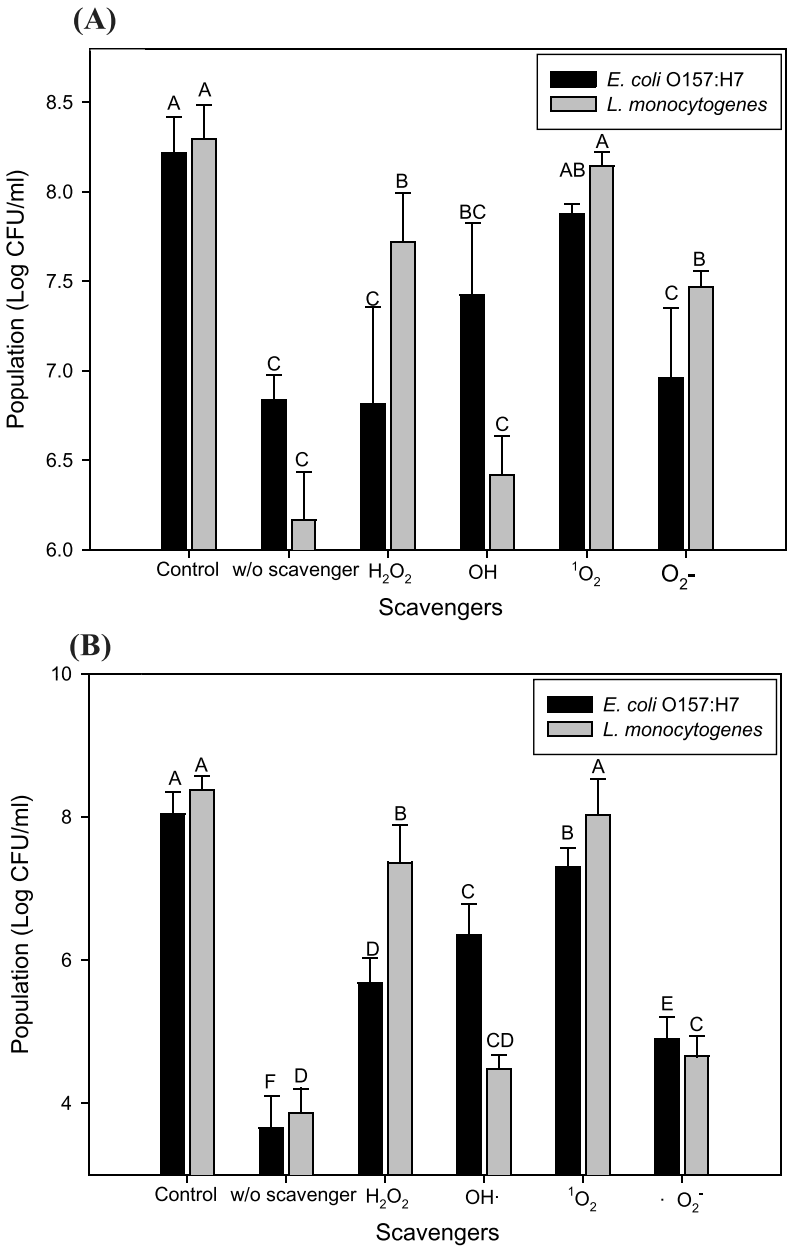

Fig. 10. Effects of ROS scavengers on photodynamic inactivation of *Escherichia coli* O157:H7 and *Listeria monocytogenes* treated with carbon quantum dots (CQDs) synthesized with malic acid, alanine, and cysteine at ratios of (A) 10:5:5 mmol (NS-CQD) and (B) 10:10:0 (N-CQD) under visible light. Sodium pyruvate (5 mM), mannitol (50 mM), sodium azide (5 mM, and Trion (5 mM) were used as scavengers of H_2O_2, $\cdot OH$, $^1O_2$, $\cdot O_2^-$, respectively. Data shown represent the averages of three independent experiments, and the error bars indicate the standard deviations. Different letters within the same pathogen indicate significant differences ($P < 0.05$).

Table 2
Specific surface area (m^2/g) of carbon quantum dots (CQDs) synthesized with malic acid, alanine, and cysteine at ratios of 10:5:5 mmol (NS-CQD), and 10:10:0 (N-CQD)

CQD	Average diameter (nm)	Density (g/cm^3)	specific surface area (m^2/g) = 6000/(D*ρ)
NS-CQD	6.95	1.51	571.73
N-CQD	4.83	1.46	850.85

D and ρ is the diameter of the particle and the density of particle, respectively.

Surface functionalization effectively induces a higher fluorescence quantum yield mainly through the Φ1 process, because it stabilizes the surface defect sites to facilitate the radiative recombination process [29,101,102]. This implies that for the same incident photon energy, the amount of emissive excited states involved in the antimicrobial activity varies according to the FLQY. Al Awak et al. (2017) showed that as the

Table 3
Fluorescence quantum yield (FLQY) of carbon quantum dots (CQDs) synthesized with malic acid, alanine, and cysteine at ratios of 10:0:0 mmol (C-CQD), 10:5:5 mmol (NS-CQD), and 10:10:0 (N-CQD).

CQD	Grad	η	FLQY (%)
Quinine sulfate	5.00×10^6	1.33	54.0
C-CQD	3.40×10^6	1.33	3.67
NS-CQD	4.67×10^6	1.33	5.04
N-CQD	1.00×10^6	1.33	10.8

FLQY is calculated as follows: $FLQY_s(Grad_x/Grad_s)(\eta_s/\eta_x)$, where 'x' and 's' refer to CQD and quinine sulfate, respectively, Grad is the slope from the plot of the integrated photoluminescence intensity versus corresponding absorbance value, and η denotes the refractive index of the solvent.

FLQY of EDA-CDs increased, the visible light-driven antimicrobial effect on Gram-positive and Gram-negative bacteria increased. Therefore, in this study, the FLQYs of C-, NS-, and N-CQD were measured and

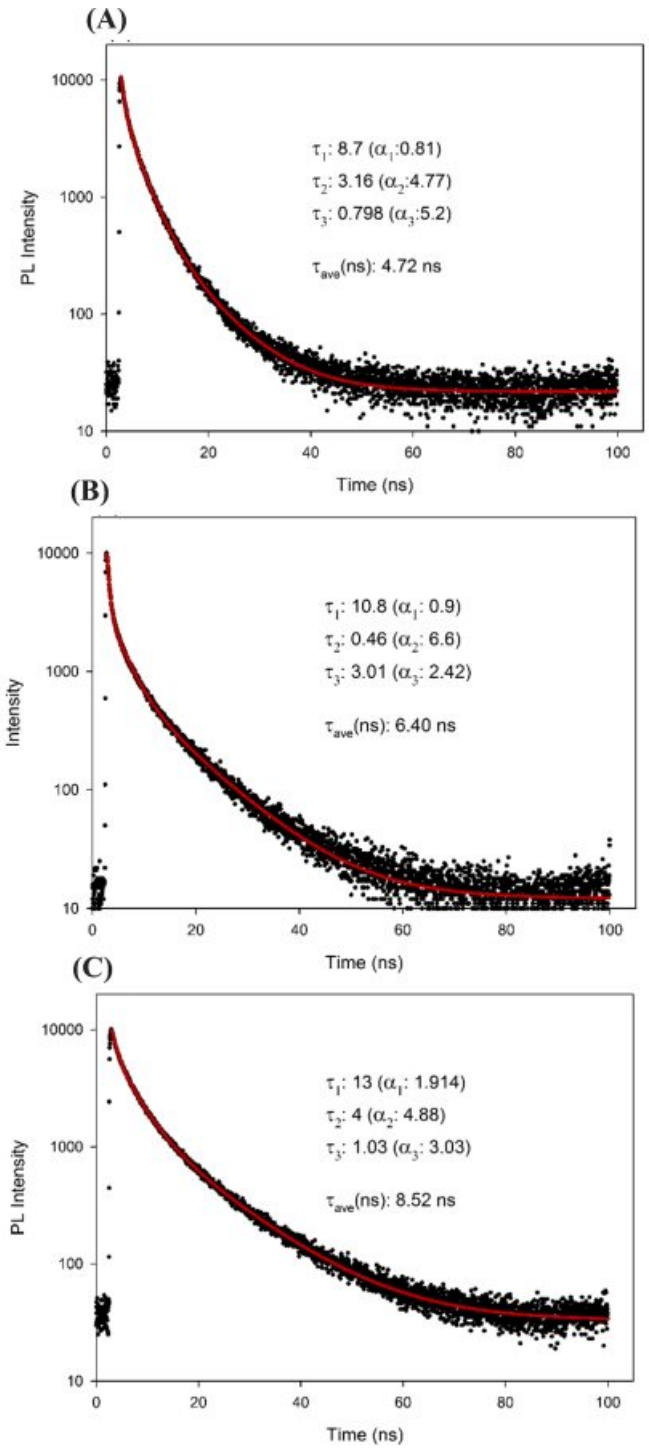

Fig. 11. The time-resolved photoluminescence (PL) decay measurements of carbon quantum dots (CQDs) synthesized with malic acid, alanine, and cysteine at ratios of (A) 10:0:0 mmol (C-CQD), (B) 10:5:5 mmol (NS-CQD), and (C) 10:10:0 (N-CQD) with excitation and emission wavelengths at 375 nm and 350 nm, respectively. Average fluorescence lifetime (τ_{ave}) was calculated using: $(a_1\tau_1^2 + a_2\tau_2^2 + a_3\tau_3^2)/(a_1\tau_1 + a_2\tau_2 + a_3\tau_3)$, where a_1, a_2, a_3 are the amplitudes as a normalized percentage (%) of the first, second, and third components, respectively, and τ_1, τ_2, and τ_3 are the PL lifetime (ns) of these components, respectively.

compared. As listed in Table 3, the FLQYs of C, NS, and N-CQD are 3.67%, 5.04%, and 10.8%, respectively, which are consistent with the antimicrobial effect results. Lu et al. (2015) synthesized undoped CDs with DL-Malic acid, N-CDs with a DL-Malic acid and Ethanolamine mixture, and S-CDs with a DL-Malic acid and Ethane sulfonic acid mixture, and found that the FLQYs of undoped CDs, N-CDs and S-CDs were 9.86%, 15.13%, and 5.51%, respectively [103]. They interpreted that these results were caused by N doping creating surface states in a form that facilitates radiative recombination, and S doping in the same manner but reversed [103]. Therefore, the results herein, in which N-CQD showed a higher visible light-driven antimicrobial effect than NS-CQD even though they have similar band gap energy, can be interpreted as N-CQD having a more easily reactive radiative recombination process that forms emissive excited states related to antimicrobial activity than NS-CQD.

3.8. PL lifetime

Zhange et al. (2018) revealed that rGOQDs have a longer fluorescence lifetime than GOQDs, resulting in higher photodynamic effects. Based on this, the PL lifetimes (τ_{ave}) of C-, NS-, and N-CQD herein were measured and compared using a time decay curve. The time decay curves of C-, NS-, and N-CQD are shown in Fig. 11 and are fitted to the following triple-exponential function: $I(t) = a_1\exp(-t/\tau_1) + a_2\exp(-t/\tau_2) + a_3\exp(-t/\tau_3)$, where a_1, a_2, *and* a_3 are the amplitudes as a normalized percentage (%) of the first, second, and third components, respectively, and τ_1, τ_2, and τ_3 are the PL lifetime (ns) of these components, respectively. The lifetimes (τ) of C-, NS-, and N-CQD are (τ_1: 8.7, τ_2: *3.16,* τ_3: 0.798), (τ_1: 10.8 τ_2: *0.46* τ_3: 3.01), and (τ_1: 13.0 τ_2: *4.0* τ_3: 1.03), respectively, and the calculated average lifetimes of C-, NS-, and N-CQDs are 4.72 ns, 6.40 ns, and 8.52 ns, respectively. These results indicate that the PL lifetime of CQDs increases with N and/or S doping, in which the increase by N doping is greater than that by NS doping. This increased PL lifetime may be related to changes in the surface states, which adjust the emission of the defect states [104]. Consequently, the duration in which the CQDs can maintain a photo-excited state can be suggested as another cause of the antimicrobial effect difference between NS- and N-CQD. That is to say, the shorter the duration of the photo-excited state, the higher the ratio to the ground state without reacting with pathogens and/or oxygen to generate ROS, thereby decreasing the antimicrobial effect.

4. Conclusions

The results of this study prove that N and/or S doping derived from amino acids (alanine and/or cysteine) enhances the VLD antimicrobial effect of CQD against Gram-positive and Gram-negative pathogenic bacteria. In particular, regarding N and S doping, as the ratio of S increased, the antimicrobial effect tended to decrease as a result of changes in the CQD characteristics that change to a photocatalytic mechanism that is disadvantageous for ROS generation, resulted in the reactive site being decreased (specific surface area increased), cause radiative recombination to be less favorable (FLQY decreased) and the photoexcitation state was less maintained (PL lifetime decreased). Consequently, the results of this study suggest that when synthesizing CQDs for high VLD antimicrobial activity using food by-products, it is useful to utilize those with a high amino acid content but a small proportion of S containing amino acids.

Declaration of Competing Interest

The authors declare that they have no known competing financial interests or personal relationships that could have appeared to influence the work reported in this paper.

Acknowledgement

This work was supported by Post-Doctoral Fellowship Program through the National Research Foundation (NRF) of South Korea funded by the Ministry of Education (No. NRF-2020R1A6A3A01099274). This work was also supported by a National Research Foundation of South Korea (NRF) grant funded by the Korean government (No. NRF-2018R1A2B2008825).

References

[1] C. Chu, E.C. Ryberg, S.K. Loeb, M.-J. Suh, J.-H. Kim, Water disinfection in rural areas demands unconventional solar technologies, Acc. Chem. Res. 52 (2019) 1187–1195.
[2] J. Song, J. Yu, G. Sun, Y. Si, B. Ding, Visible-light-driven, hierarchically heterostructured, and flexible silver/bismuth oxyiodide/titania nanofibrous membranes for highly efficient water disinfection, J. Colloid Interface Sci. 555 (2019) 636–646.
[3] W.H. Organization. Guidelines for drinking-water quality: first addendum to the fourth edition. 2017.
[4] C. Zhang, Y. Li, D. Shuai, Y. Shen, W. Xiong, L. Wang, Graphitic carbon nitride (g-C3N4)-based photocatalysts for water disinfection and microbial control: A review, Chemosphere 214 (2019) 462–479.
[5] Unicef, Progress on drinking water and sanitation: 2014 update. 2017.
[6] W. Wang, G. Li, D. Xia, T. An, H. Zhao, P.K. Wong, Photocatalytic nanomaterials for solar-driven bacterial inactivation: recent progress and challenges, Environ. Sci. Nano 4 (2017) 782–799.
[7] J. You, Y. Guo, R. Guo, X. Liu, A review of visible light-active photocatalysts for water disinfection: Features and prospects, Chem. Eng. J. 373 (2019) 624–641.
[8] X. Zeng, G. Wang, Y. Liu, X. Zhang, Graphene-based antimicrobial nanomaterials: rational design and applications for water disinfection and microbial control, Environ. Sci. Nano 4 (2017) 2248–2266.
[9] P. Pandey, B. Karki, B. Lekhak, A.R. Koirala, R. Sharma, H.R. Pant, Comparative Antibacterial Study of Silver Nanoparticles Doped Activated Carbon Prepared by Different Methods, J. Institute Eng. 15 (2019) 187–194.
[10] Y. Gilboa, E. Friedler, UV disinfection of RBC-treated light greywater effluent: kinetics, survival and regrowth of selected microorganisms, Water Res. 42 (2008) 1043–1050.
[11] X. Xu, S. Wang, X. Yu, J. Dawa, D. Gui, R. Tang, Biosynthesis of Ag deposited phosphorus and sulfur co-doped g-C3N4 with enhanced photocatalytic inactivation performance under visible light, Appl. Surf. Sci. 501 (2020), 144245.
[12] X. Zheng, Z.-P. Shen, C. Cheng, L. Shi, R. Cheng, D.-H. Yuan, Photocatalytic disinfection performance in virus and virus/bacteria system by Cu-TiO2 nanofibers under visible light, Environ. Pollut. 237 (2018) 452–459.
[13] C.-L. Hsu, Y.-J. Li, H.-J. Jian, S.G. Harroun, S.-C. Wei, R. Ravindranath, J.-Y. Lai, C.-C. Huang, H.-T. Chang, Green synthesis of catalytic gold/bismuth oxyiodide nanocomposites with oxygen vacancies for treatment of bacterial infections, Nanoscale 10 (2018) 11808–11819.
[14] W. Wang, T.W. Ng, W.K. Ho, J. Huang, S. Liang, T. An, G. Li, C.Y. Jimmy, P. K. Wong, CdIn2S4 microsphere as an efficient visible-light-driven photocatalyst for bacterial inactivation: Synthesis, characterizations and photocatalytic inactivation mechanisms, Appl. Catal. B 129 (2013) 482–490.
[15] M. Pang, J. Hu, H.C. Zeng, Synthesis, morphological control, and antibacterial properties of hollow/solid Ag2S/Ag heterodimers, J. Am. Chem. Soc. 132 (2010) 10771–10785.
[16] X. Hu, C. Hu, T. Peng, X. Zhou, J. Qu, Plasmon-induced inactivation of enteric pathogenic microorganisms with Ag− AgI/Al2O3 under visible-light irradiation, Environ. Sci. Technol. 44 (2010) 7058–7062.
[17] Z. Xiong, J. Ma, W.J. Ng, T.D. Waite, X. Zhao, Silver-modified mesoporous TiO2 photocatalyst for water purification, Water Res. 45 (2011) 2095–2103.
[18] P. Wu, R. Xie, K. Imlay, J.K. Shang, Visible-light-induced bactericidal activity of titanium dioxide codoped with nitrogen and silver, Environ. Sci. Technol. 44 (2010) 6992–6997.
[19] L. Liu, Z. Liu, H. Bai, D.D. Sun, Concurrent filtration and solar photocatalytic disinfection/degradation using high-performance Ag/TiO2 nanofiber membrane, Water Res. 46 (2012) 1101–1112.
[20] D. He, Z. Zhang, Y. Xing, Y. Zhou, H. Yang, H. Liu, J. Qu, X. Yuan, J. Guan, Y.-N. Zhang, Black phosphorus/graphitic carbon nitride: A metal-free photocatalyst for “green” photocatalytic bacterial inactivation under visible light, Chem. Eng. J. 384 (2020), 123258.
[21] X. Nie, S. Wu, A. Mensah, K. Lu, Q. Wei, Carbon quantum dots embedded electrospun nanofibers for efficient antibacterial photodynamic inactivation, Mater. Sci. Eng., C 108 (2020), 110377.
[22] M.J. Meziani, X. Dong, L. Zhu, L.P. Jones, G.E. LeCroy, F. Yang, S. Wang, P. Wang, Y. Zhao, L. Yang, Visible-light-activated bactericidal functions of carbon “Quantum” dots, ACS Appl. Mater. Interfaces 8 (2016) 10761–10766.
[23] X. Xu, R. Ray, Y. Gu, H.J. Ploehn, L. Gearheart, K. Raker, W.A. Scrivens, Electrophoretic analysis and purification of fluorescent single-walled carbon nanotube fragments, J. Am. Chem. Soc. 126 (2004) 12736–12737.
[24] Y.-P. Sun, B. Zhou, Y. Lin, W. Wang, K.S. Fernando, P. Pathak, M.J. Meziani, B. A. Harruff, X. Wang, H. Wang, Quantum-sized carbon dots for bright and colorful photoluminescence, J. Am. Chem. Soc. 128 (2006) 7756–7757.
[25] Z. Liu, H. Zou, N. Wang, T. Yang, Z. Peng, J. Wang, N. Li, C. Huang, Photoluminescence of carbon quantum dots: coarsely adjusted by quantum confinement effects and finely by surface trap states, Science China Chemistry 61 (2018) 490–496.
[26] Y. Sun, M. Zhang, B. Bhandari, C. Yang, Recent Development of Carbon Quantum Dots: Biological Toxicity, Antibacterial Properties and Application in Foods, Food Reviews International (2020) 1–20.
[27] S. Paulo, E. Palomares, E. Martinez-Ferrero, Graphene and carbon quantum dot-based materials in photovoltaic devices: From synthesis to applications, Nanomaterials 6 (2016) 157.
[28] U. Abd Rani, L.Y. Ng, C.Y. Ng, E. Mahmoudi, A review of carbon quantum dots and their applications in wastewater treatment, Adv. Colloid Interface Sci. (2020), 102124.
[29] M.M. Al Awak, P. Wang, S. Wang, Y. Tang, Y.-P. Sun, L. Yang, Correlation of carbon dots’ light-activated antimicrobial activities and fluorescence quantum yield, RSC Adv. 7 (2017) 30177–30184.
[30] A. Anand, B. Unnikrishnan, S.-C. Wei, C.P. Chou, L.-Z. Zhang, C.-C. Huang, Graphene oxide and carbon dots as broad-spectrum antimicrobial agents–a minireview, Nanoscale Horiz. 4 (2019) 117–137.
[31] P. Devi, S. Saini, K.-H. Kim, The advanced role of carbon quantum dots in nanomedical applications, Biosens. Bioelectron. 141 (2019), 111158.
[32] X. Dong, W. Liang, M.J. Meziani, Y.-P. Sun, L. Yang, Carbon dots as potent antimicrobial agents, Theranostics 10 (2020) 671.
[33] F. Lin, Y.-W. Bao, F.-G. Wu, Carbon dots for sensing and killing microorganisms, C—Journal of Carbon Research 5 (2019) 33.
[34] P. Namdari, B. Negahdari, A. Eatemadi, Synthesis, properties and biomedical applications of carbon-based quantum dots: An updated review, Biomed. Pharmacother. 87 (2017) 209–222.
[35] Y. Yan, W. Kuang, L. Shi, X. Ye, Y. Yang, X. Xie, Q. Shi, S. Tan, Carbon quantum dot-decorated TiO2 for fast and sustainable antibacterial properties under visible-light, J. Alloy. Compd. 777 (2019) 234–243.
[36] H. Fan, M. Zhang, B. Bhandari, C.-H. Yang, Food waste as a carbon source in carbon quantum dots technology and their applications in food safety detection, Trends Food Sci. Technol. 95 (2020) 86–96.
[37] X. Ren, F. Zhang, B. Guo, N. Gao, X. Zhang, Synthesis of N-doped micropore carbon quantum dots with high quantum yield and dual-wavelength photoluminescence emission from biomass for cellular imaging, Nanomaterials 9 (2019) 495.
[38] R. Das, R. Bandyopadhyay, P. Pramanik, Carbon quantum dots from natural resource: A review, Mater. Today Chem. 8 (2018) 96–109.
[39] C.-C. Huang, Y.-S. Hung, Y.-M. Weng, W. Chen, Y.-S. Lai, Sustainable development of carbon nanodots technology: Natural products as a carbon source and applications to food safety, Trends Food Sci. Technol. 86 (2019) 144–152.
[40] X. Kou, S. Jiang, S.-J. Park, L.-Y. Meng, A review: recent advances in preparations and applications of heteroatom-doped carbon quantum dots, Dalton Trans. 49 (2020) 6915–6938.
[41] S. Miao, K. Liang, J. Zhu, B. Yang, D. Zhao, B. Kong, Hetero-atom-doped carbon dots: Doping strategies, properties and applications, Nano Today 33 (2020), 100879.
[42] T.L. Wilson, M.J. Guttieri, N.O. Nelson, A. Fritz, M. Tilley, Nitrogen and sulfur effects on hard winter wheat quality and asparagine concentration, J. Cereal Sci. 102969 (2020).
[43] J.-W. Kang, S.-S. Kim, D.-H. Kang, Inactivation dynamics of 222 nm krypton-chlorine excilamp irradiation on Gram-positive and Gram-negative foodborne pathogenic bacteria, Food Res. Int. 109 (2018) 325–333.
[44] S.O. Liubimovskii, L.Y. Ustynyuk, A.N. Tikhonov, Superoxide radical scavenging by sodium 4, 5-dihydroxybenzene-1, 3-disulfonate dissolved in water: Experimental and quantum chemical studies, J. Mol. Liq. 115810 (2021).
[45] R. Franco, M.I. Panayiotidis, J.A. Cidlowski, Glutathione depletion is necessary for apoptosis in lymphoid cells independent of reactive oxygen species formation, J. Biol. Chem. 282 (2007) 30452–30465.
[46] Y. Yang, X. Lin, W. Li, J. Ou, Z. Yuan, F. Xie, W. Hong, D. Yu, Y. Ma, Z. Chi, One-pot large-scale synthesis of carbon quantum dots: efficient cathode interlayers for polymer solar cells, ACS Appl. Mater. Interfaces 9 (2017) 14953–14959.
[47] H.-X. Wang, J. Xiao, Z. Yang, H. Tang, Z.-T. Zhu, M. Zhao, Y. Liu, C. Zhang, H.-L. Zhang, Rational design of nitrogen and sulfur co-doped carbon dots for efficient photoelectrical conversion applications, J. Mater. Chem. A 3 (2015) 11287–11293.
[48] H.J. Yvon, A Guide to Recording Fluorescence Quantum Yields, HORIBA Jobin Yvon Inc., Stanmore, Middlesex, UK, 2012.
[49] B. De, K. Gupta, M. Mandal, N. Karak, Biocide immobilized OMMT-carbon dot reduced Cu2O nanohybrid/hyperbranched epoxy nanocomposites: Mechanical, thermal, antimicrobial and optical properties, Mater. Sci. Eng., C 56 (2015) 74–83.
[50] J. Liu, H. Zhang, D. Tang, X. Zhang, L. Yan, Y. Han, H. Huang, Y. Liu, Z. Kang, Carbon quantum dot/silver nanoparticle/polyoxometalate composites as photocatalysts for overall water splitting in visible light, ChemCatChem 6 (2014) 2634–2641.
[51] X. Deng, Y. Feng, H. Li, Z. Du, Q. Teng, H. Wang, N-doped carbon quantum dots as fluorescent probes for highly selective and sensitive detection of Fe3+ ions, Particuology 41 (2018) 94–100.
[52] P. Mandal, J. Debbarma, M. Saha, One Step Synthesis of N-Containing Graphene Oxide from 3-Aminophenol, Cryst. Res. Technol. 55 (2020) 1900158.
[53] Z. Wu, L. Wang, Graphene oxide (GO) doping hexagonal flower-like ZnO as potential enhancer of photocatalytic ability, Mater. Lett. 234 (2019) 287–290.

[54] M. Naushad, T. Ahamad, G. Sharma, H. Ala'a, A.B. Albadarin, M.M. Alam, Z. A. ALOthman, S.M. Alshehri, A.A. Ghfar, Synthesis and characterization of a new starch/SnO2 nanocomposite for efficient adsorption of toxic Hg2+ metal ion, Chem. Eng. J. 300 (2016) 306–316.
[55] S. Wang, Y. Zhu, B. Liu, C. Wang, R. Ma, Introduction of carbon nanodots into SnO 2 electron transport layer for efficient and UV stable planar perovskite solar cells, J. Mater. Chem. A 7 (2019) 5353–5362.
[56] J.-J. Feng, L.-X. Chen, P. Song, X.-L. Wu, A.-J. Wang, J. Yuan, Bimetallic AuPd nanoclusters supported on graphitic carbon nitride: one-pot synthesis and enhanced electrocatalysis for oxygen reduction and hydrogen evolution, Int. J. Hydrogen Energy 41 (2016) 8839–8846.
[57] B. Ramezanzadeh, B. Karimi, M. Ramezanzadeh, M. Rostami, Synthesis and characterization of polyaniline tailored graphene oxide quantum dot as an advance and highly crystalline carbon-based luminescent nanomaterial for fabrication of an effective anti-corrosion epoxy system on mild steel, J. Taiwan Inst. Chem. Eng. 95 (2019) 369–382.
[58] Y. Zhang, S. Tian, C. Yang, J. Nan, Three-dimensional nitrogen–sulfur codoped layered porous carbon nanosheets with sulfur-regulated nitrogen content as a high-performance anode material for potassium-ion batteries, Dalton Trans. 49 (2020) 5108–5120.
[59] K. Xu, Y. Li, J. Xiong, X. Ou, W. Su, G. Zhong, C. Yang, Activated amorphous carbon with high-porosity derived from camellia pollen grains as anode materials for lithium/sodium ion batteries, Front. Chem. 6 (2018) 366.
[60] R. Atchudan, T.N.J.I. Edison, M.G. Sethuraman, Y.R. Lee, Efficient synthesis of highly fluorescent nitrogen-doped carbon dots for cell imaging using unripe fruit extract of Prunus mume, Appl. Surf. Sci. 384 (2016) 432–441.
[61] A. Byeon, C. Hatter, J.H. Park, C.W. Ahn, Y. Gogotsi, J.W. Lee, Molybdenum oxide/carbon composites derived from the CO2 oxidation of Mo2CTx (MXene) for lithium ion battery anodes, Electrochim. Acta 258 (2017) 979–987.
[62] H. Yuan, B. Qian, W. Zhang, M. Lan, Protein adsorption resistance of PVP-modified polyurethane film prepared by surface-initiated atom transfer radical polymerization, Appl. Surf. Sci. 363 (2016) 483–489.
[63] N. Parveen, N. Mahato, M.O. Ansari, M.H. Cho, Enhanced electrochemical behavior and hydrophobicity of crystalline polyaniline@ graphene nanocomposite synthesized at elevated temperature, Compos. B Eng. 87 (2016) 281–290.
[64] L. Chai, W. Yuan, X. Cui, H. Jiang, J. Tang, X. Guo, Surface engineering-modulated porous N-doped rod-like molybdenum phosphide catalysts: towards high activity and stability for hydrogen evolution reaction over a wide pH range, RSC Adv. 8 (2018) 26871–26879.
[65] H.R. Naderi, A. Sobhani-Nasab, M. Rahimi-Nasrabadi, M.R. Ganjali, Decoration of nitrogen-doped reduced graphene oxide with cobalt tungstate nanoparticles for use in high-performance supercapacitors, Appl. Surf. Sci. 423 (2017) 1025–1034.
[66] B.J. Kim, D.U. Lee, J. Wu, D. Higgins, A. Yu, Z. Chen, Iron-and nitrogen-functionalized graphene nanosheet and nanoshell composites as a highly active electrocatalyst for oxygen reduction reaction, J. Phy. Chem. C 117 (2013) 26501–26508.
[67] J. Jiang, L. Zhu, H. Chen, Y. Sun, W. Qian, H. Lin, S. Han, Highly active and stable electrocatalysts of FeS 2–reduced graphene oxide for hydrogen evolution, J. Mater. Sci. 54 (2019) 1422–1433.
[68] G. Li, D. Luo, X. Wang, M.H. Seo, S. Hemmati, A. Yu, Z. Chen, Enhanced reversible sodium-ion intercalation by synergistic coupling of few-layered MoS2 and S-doped graphene, Adv. Funct. Mater. 27 (2017) 1702562.
[69] Y. Zhang, Z. Jin, Synergistic Enhancement of Hydrogen Production by ZIF-67 (Co) Derived Mo–Co–S Modified gC 3 N 4/rGO Photocatalyst, Catal. Lett. 149 (2019) 34–48.
[70] K. Deng, T. Gao, Q. Fang, F. Wu, C. Lu, F. Zhang, W. Cao, M. Han, C. Hu, L. Lyu, Vanadium tetrasulfide cross-linking graphene-like carbon driving a sustainable electron supply chain from pollutants through the activation of dissolved oxygen and hydrogen peroxide, Environ. Sci. Nano 8 (2021) 86–96.
[71] S. Liu, W. Wang, Y. Hu, F. Tian, X. Miao, L. Liu, Z. Xu, Hetero-shaped coral-like catalysts through metal-support interaction between nitrogen-doped graphene quantum dots and PtPd alloy for oxygen reduction reaction, Electrochim. Acta 364 (2020), 137314.
[72] J. Long, K. Shen, L. Chen, Y. Li, Multimetal-MOF-derived transition metal alloy NPs embedded in an N-doped carbon matrix: highly active catalysts for hydrogenation reactions, J. Mater. Chem. A 4 (2016) 10254–10262.
[73] X. Dong, A.E. Bond, N. Pan, M. Coleman, Y. Tang, Y.-P. Sun, L. Yang, Synergistic photoactivated antimicrobial effects of carbon dots combined with dye photosensitizers, Int. J. Nanomed. 13 (2018) 8025.
[74] D.I.A. Rabe, M.M. Al Awak, F. Yang, P.A. Okonjo, X. Dong, L.R. Teisl, P. Wang, Y. Tang, N. Pan, Y.-P. Sun, The dominant role of surface functionalization in carbon dots' photo-activated antibacterial activity, Int. J. Nanomed. 14 (2019) 2655.
[75] Y. Sun, C. Shen, J. Wang, Y. Lu, Facile synthesis of biocompatible N, S-doped carbon dots for cell imaging and ion detecting, RSC, Advances 5 (2015) 16368–16375.
[76] J. Liu, X. Liu, H. Luo, Y. Gao, One-step preparation of nitrogen-doped and surface-passivated carbon quantum dots with high quantum yield and excellent optical properties, RSC Adv. 4 (2014) 7648–7654.
[77] N. Li, F. Lei, D. Xu, Y. Li, J. Liu, Y. Shi, One-step synthesis of N, P Co-doped orange carbon quantum dots with novel optical properties for bio-imaging, Opt. Mater. (2020), 110618.
[78] H. Wang, P. Sun, S. Cong, J. Wu, L. Gao, Y. Wang, X. Dai, Q. Yi, G. Zou, Nitrogen-doped carbon dots for "green" quantum dot solar cells, Nanoscale Res. Lett. 11 (2016) 1–6.
[79] T.K. Mondal, S.K. Saha, Facile approach to synthesize nitrogen-and oxygen-rich carbon quantum dots for pH sensor, fluorescent indicator, and invisible ink applications, ACS Sustain. Chem. Eng. 7 (2019) 19669–19678.
[80] J. Yu, C. Xu, Z. Tian, Y. Lin, Z. Shi, Facilely synthesized N-doped carbon quantum dots with high fluorescent yield for sensing Fe 3+, New J. Chem. 40 (2016) 2083–2088.
[81] U. Abd Rani, L.Y. Ng, C.Y. Ng, E. Mahmoudi, Y.-S. Ng, A.W. Mohammad, Sustainable production of nitrogen-doped carbon quantum dots for photocatalytic degradation of methylene blue and malachite green, Journal of Water, Process Eng. (2020), 101816.
[82] W.J. Lee, J. Lim, S.O. Kim, Nitrogen dopants in carbon nanomaterials: defects or a new opportunity, Small Method. 1 (2017) 1600014.
[83] X. Dong, L. Ge, D.I.A. Rabe, O.O. Mohammed, P. Wang, Y. Tang, S. Kathariou, L. Yang, Y.-P. Sun, Photoexcited state properties and antibacterial activities of carbon dots relevant to mechanistic features and implications, Carbon 170 (2020) 137–145.
[84] C.J. Hewitt, G. Nebe-Von-Caron, The application of multi-parameter flow cytometry to monitor individual microbial cell physiological state, Physiol. Stress Respons. Bioproces. (Springer 2004,) 197–223.
[85] P. Breeuwer, T. Abee, Assessment of viability of microorganisms employing fluorescence techniques, Int. J. Food Microbiol. 55 (2000) 193–200.
[86] E. Sánchez, S. García, N. Heredia, Extracts of edible and medicinal plants damage membranes of Vibrio cholerae, Appl. Environ. Microbiol. 76 (2010) 6888–6894.
[87] R. Pagán, B. Mackey, Relationship between membrane damage and cell death in pressure-treated *Escherichia coli* cells: differences between exponential-and stationary-phase cells and variation among strains, Appl. Environ. Microbiol. 66 (2000) 2829–2834.
[88] T. Kaneda, Iso-and anteiso-fatty acids in bacteria: biosynthesis, function, and taxonomic significance, Microbiol. Mol. Biol. Rev. 55 (1991) 288–302.
[89] J. Gutteridge, Lipid peroxidation and antioxidants as biomarkers of tissue damage, Clin. Chem. 41 (1995) 1819–1828.
[90] Y. Okimoto, A. Watanabe, E. Niki, T. Yamashita, N. Noguchi, A novel fluorescent probe diphenyl-1-pyrenylphosphine to follow lipid peroxidation in cell membranes, FEBS Lett. 474 (2000) 137–140.
[91] I.O. Bacellar, M.C. Oliveira, L.S. Dantas, E.B. Costa, H.C. Junqueira, W.K. Martins, A.s.M. Durantini, G. Cosa, P. Di Mascio, M. Wainwright, Photosensitized membrane permeabilization requires contact-dependent reactions between photosensitizer and lipids, J. Am. Chem. Soc. 140 (2018) 9606–9615.
[92] L. Xiong, J. Tang, Strategies and Challenges on Selectivity of Photocatalytic Oxidation of Organic Substances, Adv. Energy Mater. 11 (2021) 2003216.
[93] M.D.G. de Luna, L.K.B. Paragas, R.-A. Doong, Insights into the rapid elimination of antibiotics from aqueous media by tunable C3N4 photocatalysts: Effects of dopant amount, co-existing ions and reactive oxygen species, Sci. Total Environ. 669 (2019) 1053–1061.
[94] L. Huang, Y. Xuan, Y. Koide, T. Zhiyentayev, M. Tanaka, M.R. Hamblin, Type I and Type II mechanisms of antimicrobial photodynamic therapy: an in vitro study on gram-negative and gram-positive bacteria, Lasers Surg. Med. 44 (2012) 490–499.
[95] S.H. Jin, D.H. Kim, G.H. Jun, S.H. Hong, S. Jeon, Tuning the photoluminescence of graphene quantum dots through the charge transfer effect of functional groups, ACS Nano 7 (2013) 1239–1245.
[96] P. Niu, L. Zhang, G. Liu, H.M. Cheng, Graphene-like carbon nitride nanosheets for improved photocatalytic activities, Adv. Funct. Mater. 22 (2012) 4763–4770.
[97] Q. Zhang, X. Xu, Y. Liu, M. Xu, S. Deng, Y. Chen, H. Yuan, F. Yu, Y. Huang, K. Zhao, A feasible strategy to balance the crystallinity and specific surface area of metal oxide nanocrystals, Sci. Rep. 7 (2017) 1–12.
[98] S.J. Hong, H. Jun, P.H. Borse, J.S. Lee, Size effects of WO3 nanocrystals for photooxidation of water in particulate suspension and photoelectrochemical film systems, Int. J. Hydrogen Energy 34 (2009) 3234–3242.
[99] B. Bera, A. Chakraborty, T. Kar, P. Leuaa, M. Neergat, Density of states, carrier concentration, and flat band potential derived from electrochemical impedance measurements of N-doped carbon and their influence on electrocatalysis of oxygen reduction reaction, J. Phy. Chem. C 121 (2017) 20850–20856.
[100] I.A. Wani, A. Ganguly, J. Ahmed, T. Ahmad, Silver nanoparticles: ultrasonic wave assisted synthesis, optical characterization and surface area studies, Mater. Lett. 65 (2011) 520–522.
[101] F. Yang, G.E. LeCroy, P. Wang, W. Liang, J. Chen, K.S. Fernando, C.E. Bunker, H. Qian, Y.-P. Sun, Functionalization of Carbon Nanoparticles and Defunctionalization Toward Structural and Mechanistic Elucidation of Carbon "Quantum" Dots, the, J. Phys. Chem. C 120 (2016) 25604–25611.
[102] L. Cao, M.J. Meziani, S. Sahu, Y.-P. Sun, Photoluminescence properties of graphene versus other carbon nanomaterials, Acc. Chem. Res. 46 (2013) 171–180.
[103] W. Lu, X. Gong, M. Nan, Y. Liu, S. Shuang, C. Dong, Comparative study for N and S doped carbon dots: synthesis, characterization and applications for Fe3+ probe and cellular imaging, Anal. Chim. Acta 898 (2015) 116–127.
[104] S.K. Lai, C.M. Luk, L. Tang, K.S. Teng, S.P. Lau, Photoresponse of polyaniline-functionalized graphene quantum dots, Nanoscale 7 (2015) 5338–5343.